Eleventh International Conference on Computational Fluid Dynamics (ICCFD11), Maui, Hawaii, July 11-15, 2022

ICCFD11-2022-3702

Vortex Structure Analysis Method for Separated Shear Flow

Takuto Ogawa*, Tomoaki Tatsukawa* and Kozo Fujii*
Corresponding author: 4418701@ed.tus.ac.jp

* Tokyo University of Science, Japan.

Abstract: The objective in this study is to establish a vortex structures analysis method for the large-eddy simulation (LES) data. We proposed a new technique to identify fine-scale vortices (resolved vortices) by extracting vortex filaments from LES data and evaluate their feature values, such as the location, volume, and vorticity components. To investigate the effectiveness of the proposed method, the propose method was applied to actual LES dataset that is a transient flow around an airfoil, which is controlled by a DBD plasma actuator. As a result, the vortex filaments and resolved vortices ware successfully identified and their feature values were evaluated. The effectiveness of the proposed method was verified by conducting characteristic analysis of steady flow and time variation analysis of unsteady flow, which could not be realized by the conventional method by using the feature values.

Keywords: Data analysis, Vortex structure, Transient flow, DBD plasma actuator, Large-eddy simulation Computational fluid dynamics.

1 Introduction

Vortex is one of the most important elements for analyzing the fluid flow phenomena. In the engineering field, the characteristics of the vortex structure are analyzed to evaluate the performance and safety of machinery. To identify vortex structures from numerical data, various definitions have been studied [1–4]. In most cases, vortex structures are visualized and qualitatively evaluated using, the second invariant of the velocity gradient tensor (Q^*), the eigenvalue of the pressure Hessian, and the spatial modes of POD computed for the velocity field are used [1, 4, 6]. However, in the unsteady or complicated turbulent flow condition, it is difficult to evaluate the influence of the vortex structure on the flow and the machinery only by using the conventional visualization analysis method. This is because the vortex structures are complexly united, split, and disappear. Therefore, fine-scale vortex [5, 6] are extracted individually, and characteristics of them are quantitatively evaluated. Wang et al. [7] studied the location and characteristics of coherent fine vortices in the turbulent flow. They proposed the extraction method for vortex filament [8] of coherent fine vortices from the turbulent flow and evaluated the distribution and direction of vortices against the free-stream. Makihara et al. [9] studied the time variation of coherent fine vortices in the homogeneous isotropic turbulence. They proposed the automatic tracking scheme for coherent fine vortices, which move individually with respect to each other, and evaluated the interaction between vortices. Most of these extraction methods are based on the numerical data of the direct numerical simulation (DNS) because these require high spatial and time resolutions to resolve a fine-scale vortex. If these methods are directly applied to numerical data with a resolution lower than the DNS data, the shape of the vortex may be mistakenly identified. In addition, the flow condition of numerical data for the these methods requires low Reynolds number. This is because the method uses the vorticity vector at a point with a high reference value, such as Q^*, to estimate the shape of the vortex filament. If these methods are directly applied to numerical data with the high Reynolds number where the shear layer is massively developed, the shape of the vortex filament may be mistakenly extracted. Liu et al. [10] proposed "Rortex" as an approach that is possible to solve the problem, but it is not possible to use widely used Q^* or vorticity because it is necessary to introduce a new physical criteria. Moreover, these methods is only for analyzing the vortex. To evaluate the effects of the vortex on the flow and machinery in more detail, it is necessary to analyze the interaction between vortices and other structures. Therefore, the analysis method that can identify and quantitatively evaluate vortices and other structures is required.

Our final goal is to establish an analysis method that can identify and quantitatively evaluate vortices and other structures from the LES data. In this study, we propose an analysis method that identifies and analyzes the vortex filaments and fine-scale vortices (Hereinafter, it is called "resolved vortices" that are the fine-scale vortices resolved by each numerical calculation.). The proposed method has unique features that can be applied to a dataset that does not necessarily resolve all vortices, such as LES dataset. In addition, it is possible to effectively extract the feature values of the vortex structure in shear flow since the proposed method is based on Q^*. Furthermore, the proposed method provides data compression because it extracts and stores the feature values of the vortex structures on a line. By using the obtained feature values, it is possible to perform characteristic analysis for steady flow and time variation analysis for unsteady flow, as well as statistical analysis and cluster analysis. In this study, to investigate the effectiveness of the proposed method, the proposed method is applied to actual LES dataset that is a transient flow around an airfoil. The vortex filaments and resolved vortices are identified and analyzed by using their location, volume, and vorticity components.

2 A new vortex analysis method

Here, we present the detailed procedure of the new vortex analysis method. First, we describes the identification method of the vortex filament and resolved vortex in the subsection 2.1, and then the analysis method of the vortex filament and resolved vortex in the subsection 2.2. Each method does not require much computational resources and can be calculated on a regular desktop or laptop like any other method.

2.1 Identification of the vortex filament and resolved vortex

The new identification method proposed in this study consists of five steps. At each step, the second invariant of the velocity gradient tensor (Q^*) is used as a physical criterion for processing the dataset. The dataset is transformed into a tree structure based on Q^* before Step 3 which is the main processing step. Therefore, the dataset has no dimensional constraints. The explanation of the method is described with two-dimensional dataset for easier understanding. However, the approach can be easily expanded for the three-dimensional dataset.

(Step 1) First, the vortex and nonvortex structure regions are determined. Q^* is evaluated at every reference point in the numerical dataset. Q^* is formulated as follows:

$$Q^* = \frac{1}{2}({\mathit{\Omega}_{\mathrm{ij}}}^2 - {S_{\mathrm{ij}}}^2), \tag{1}$$

where S_{ij} and $\mathit{\Omega}_{\mathrm{ij}}$ are the symmetric and asymmetric components of the second-order velocity gradient tensor D_{ij}, respectively. They are formulated as follows:

$$\mathit{\Omega}_{\mathrm{ij}} = \frac{1}{2}(\frac{\partial u_{\mathrm{i}}}{\partial x_{\mathrm{j}}} - \frac{\partial u_{\mathrm{j}}}{\partial x_{\mathrm{i}}}), \tag{2}$$

$$S_{\mathrm{ij}} = \frac{1}{2}(\frac{\partial u_{\mathrm{i}}}{\partial x_{\mathrm{j}}} + \frac{\partial u_{\mathrm{j}}}{\partial x_{\mathrm{i}}}), \tag{3}$$

$$D_{\mathrm{ij}} = S_{\mathrm{ij}} + \mathit{\Omega}_{\mathrm{ij}}, \tag{4}$$

where x and u are the coordinate and velocity components, respectively; S_{ij} is also called the deformation rate tensor, which is an indicator of the deformation motion of fluid elements; $\mathit{\Omega}_{\mathrm{ij}}$ is also called the rotation rate tensor, which is an indicator of the rotational motion of fluid elements. In this study, Q^* is evaluated on every grid point except wall boundary. Regions where the rotational motion exceeds the deformation motion ($Q^* > 0$) are defined as the vortex structures, while regions where the deformation motion exceeds the rotational motion ($Q^* \leq 0$) are defined to as the non-vortex structures. In this study, we focus only on the regions of the vortex structure. Note that this threshold value can be adjusted if the method is applied to noisy datasets. Figure 1 shows the computational diagram of the vortex structure region.

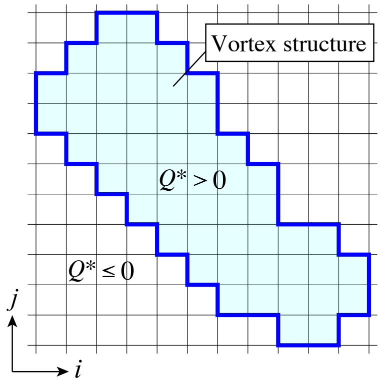

Figure 1 Determination of the vortex structure region with the second invariant of the velocity gradient tensor (Q^*).

(Step 2) Next, the minimum configurations in the vortex structure are constructed. An arbitrary reference point is selected as $\mathrm{P_a}$. Among all points that are adjacent to $\mathrm{P_a}$, the point where a value of an evaluation index is the highest and higher than value at $\mathrm{P_a}$ is selected as $\mathrm{P_b}$. The evaluation index needs to be adjusted according to the target to be analyzed. In this study, the evaluation index is a spatial gradient of Q^*. If the dataset is two-dimensional or three-dimensional cartesian grid data, then the total number of adjacent points is $3^2 - 1$ and $3^3 - 1$, respectively. Hereinafter, every point is regarded as a node of the tree structure. An edge between $\mathrm{P_a}$ and $\mathrm{P_b}$ is created, as shown in Fig. 2(a). $\mathrm{P_a}$ and $\mathrm{P_b}$ are a child and a parent node, respectively.

By performing this process on every node, multiple tree structures are constructed in each of the vortex structures, as shown in Fig. 2(b). Each tree structure is defined as unit U ($\{\mathrm{U_N}|\mathrm{N} = 1, 2, 3, ...\}$) which is the minimum configuration of the vortex structure. Nodes without a parent node are the local maximum points of Q^* and defined as the root node R ($\{\mathrm{R_N}|\mathrm{N} = 1, 2, 3, ...\}$) of the unit. Nodes without a child node are defined as leaf nodes L ($\{\mathrm{L_{NM}}|\mathrm{M}, \mathrm{N} = 1, 2, 3, ...\}$) of the unit. In each unit, it is possible to reach to the single root node by tracing its parent node from an arbitrarily selected node. In other words, this method not only constructs the units, but also detects the root node by rooting back. Each node is given a unit number. If the unit numbers of adjacent nodes are different, the unit boarder is defined between these points.

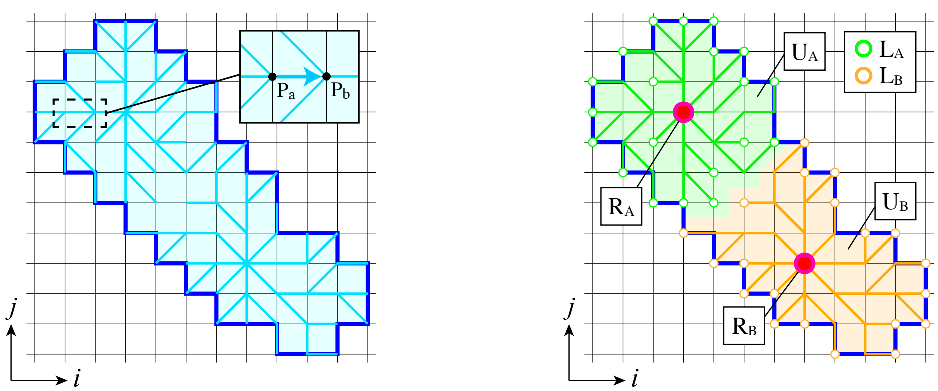

(a) Construction of edges based on the magnitude relationship between Q^* of each adjacent reference points (nodes).

(b) Construction of the tree structures (units).

Figure 2 Construction of the tree structures (units) based on Q^*.

This process is similar to dividing a mountain range into independent mountains. The vortex structure is equivalent to a mountain range. The unit is equivalent to an independent mountain in the mountain range. The edge is equivalent to a route that reaches a ridge line as quickly as possible by searching the neighborhood from an arbitrary point, and finally reaches a vertex of the mountain.

(Step 3) The path integral values of Q^* on every path in each unit are compared to estimate the path of the vortex filament. An arbitrary unit is selected as $\mathrm{U_A}$. The root and leaf nodes in $\mathrm{U_A}$ are defined as $\mathrm{R_A}$ and $\mathrm{L_A}$ ($\{\mathrm{L_{AM}}|\mathrm{M}=1,2,3,...\}$), respectively. The path integral value of Q^* from $\mathrm{R_A}$ to each leaf node is evaluated. Note that the values between nodes are linearly interpolated in the path integration. The paths with the highest path integral value of Q^* are saved as $\mathrm{E_A}$ ($\{\mathrm{E_{AM}}|\,0\le \mathrm{M}\le 2\}$) in order, as shown in Fig. 3. $\mathrm{E_A}$ are paths where the rotational motion greatly exceeds the deformation motion in the unit. $\mathrm{E_A}$ do not have common nodes other than $\mathrm{R_A}$. The leaf nodes contained in $\mathrm{E_A}$ are called $\mathrm{T_A}$ ($\{\mathrm{T_{AM}}|\,0\le \mathrm{M}\le 2\}$). In this study, these paths are defined as the candidates of the vortex filament. This process is performed on every unit.

(Step 4) The path integral values of Q^* on every paths between the adjacent units are compared to estimate the path of the vortex filament. The two units are defined as adjacent if any of the nodes are adjacent. The path with the maximum path integral value of Q^* between the root nodes of the adjacent units is extracted. $\mathrm{U_A}$ and $\mathrm{U_B}$ are adjacent via $\mathrm{N_{AB}}$ ($\{\mathrm{N_{ABM}}|\mathrm{M}=1,2,3,...\}$) and $\mathrm{N_{BA}}$ ($\{\mathrm{N_{BAM}}|\mathrm{M}=1,2,3,...\}$). $\mathrm{N_{AB}}$ and $\mathrm{N_{BA}}$ are not necessarily the leaf nodes. The path integral values from $\mathrm{R_A}$ to $\mathrm{N_{AB}}$, from $\mathrm{N_{AB}}$ to $\mathrm{N_{BA}}$ and from $\mathrm{N_{BA}}$ to $\mathrm{R_B}$ are evaluated. Note that the values between nodes are linearly interpolated in the path integration. The path with the maximum path integral value Q^*_{EAB} is saved as the candidates of the vortex filament $\mathrm{E_{AB}}$, as shown in Fig. 4. A midpoint between $\mathrm{N_{AB}}$ and $\mathrm{N_{BA}}$ is defined as $\mathrm{B_{AB}}$.

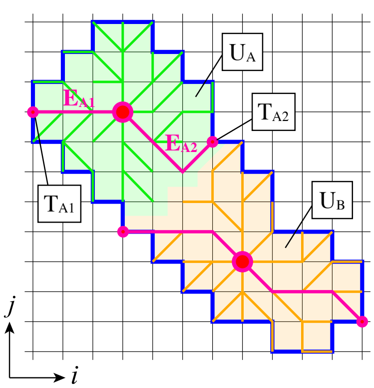

Figure 3 Path selection based on the path integral value of Q^* in each unit.

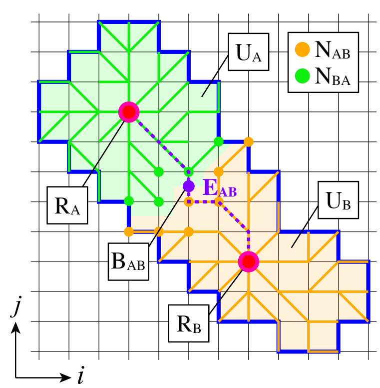

Figure 4 Path selection based on the path integral value of Q^* in the adjacent units.

(Step 5) In step 5, the magnitude relationships of the paths extracted in the previous steps are compared, and the larger path are retained. The leaf nodes that are closest to $\mathrm{B_{AB}}$ in $\mathrm{T_A}$ and $\mathrm{T_B}$ are called $\mathrm{T_{A'}}$ and $\mathrm{T_{B'}}$, respectively. The path from $\mathrm{T_{A'}}$ and $\mathrm{T_{B'}}$ to the respective root nodes are called $\mathrm{E_{A'}}$ and $\mathrm{E_{B'}}$, respectively. In Fig. 5, $\mathrm{T_{A'}}$, $\mathrm{T_{B'}}$, $\mathrm{E_{A'}}$ and $\mathrm{E_{B'}}$ are $\mathrm{T_{A2}}$, $\mathrm{T_{B1}}$, $\mathrm{E_{A2}}$ and $\mathrm{E_{B1}}$, respectively. The path integral values of the Q^* on $\mathrm{E_{A'}}$ and $\mathrm{E_{B'}}$ are evaluated as $Q^*_{\mathrm{EA'}}$ and $Q^*_{\mathrm{EB'}}$, respectively. $Q^*_{\mathrm{EA'}}$ and $Q^*_{\mathrm{EB'}}$ are compared with Q^*_{EAB}. In the case where Q^*_{EAB} is greater than both $Q^*_{\mathrm{EA'}}$ and $Q^*_{\mathrm{EB'}}$, $\mathrm{E_{A'}}$ and $\mathrm{E_{B'}}$ are deleted, while $\mathrm{E_{AB}}$ is retained, as shown in Fig. 5. $\mathrm{U_A}$ and $\mathrm{U_B}$ are combined and defined as one resolved vortex. The retained and shared path is defined as one vortex filament. In other case where Q^*_{EAB} is less than either $Q^*_{\mathrm{EA'}}$ or $Q^*_{\mathrm{EB'}}$, $\mathrm{E_{A'}}$ and $\mathrm{E_{B'}}$ are retained, while $\mathrm{E_{AB}}$ is deleted. $\mathrm{U_A}$ and $\mathrm{U_B}$ are not combined and defined as two different resolved vortices. The each retained paths are defined as vortex filament.

It should be noted that if there are multiple adjacent units, the path constructed by this process depends on the order of the adjacent units in which the process is performed. This is because if are multiple paths between adjacent units, which causes branching in the path, it is necessary to decide which path to be retained. Therefore, Step 4 is performed in advance for all adjacent units and this process is performed in the order from the adjacent paths with the higher path integral value of Q^*. If the branch occurs in the already retained path due to the connection of a new arbitrary path, that path is deleted. In Fig. 6, $\mathrm{E_{CD}}$ and $\mathrm{E_{DE}}$ are already retained, therefore $\mathrm{E_{DF}}$ is deleted (Q^*_{ECD}, $Q^*_{\mathrm{EDE}} > Q^*_{\mathrm{EDF}}$).

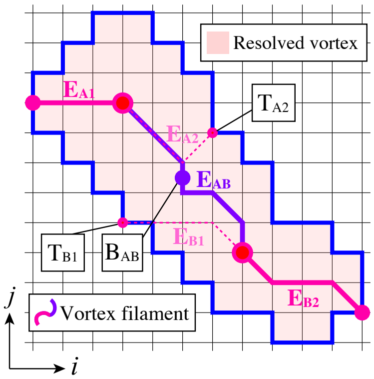

Figure 5 Determination of the vortex filament path and the resolved vortex region.

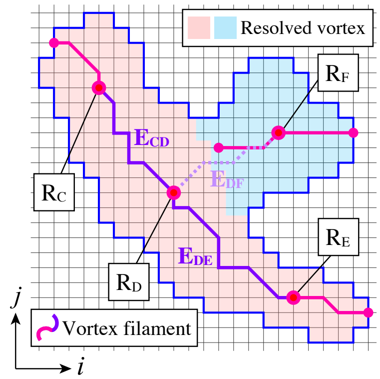

Figure 6 Disconnecting of the vortex filament paths which are branched.

In this study, the retained paths are defined as the vortex filaments and the sets of units that share a particular vortex filament are defined as the resolved vortices. The vortex structure which is shown in Fig. 5 consists of two units, one vortex filament, and one resolved vortex. The vortex structure which is shown in Fig. 6 consists of four units, two vortex filaments, and two resolved vortices.

2.2 Analysis method for vortex filament and resolved vortex

The physical quantities in the vortex filaments and resolved vortices, which are extracted by the process in the subsection 2.1, are evaluated. The physical quantities are used for the analysis as representative quantities of resolved vortices. In this study, the center of gravity G and volume V of the resolved vortices and the vorticity vector $\boldsymbol{\omega}$ and its components $(\omega_x, \omega_y, \omega_z)$ of the vortex filaments are evaluated. The components of vectors, such as vorticity, are possible to underestimate if they are simply integrated. Therefore, the vector components are divided into positive and negative values. For example, the vorticity vector $\boldsymbol{\omega} = (\omega_x, \omega_y, \omega_z)$ is divided into $(\omega_{-x,+x}, \omega_{-y,+y}, \omega_{-z,+z})$ as follows:

$$\omega_{-i}(x,y,z) = \begin{cases} 0 & (\omega_i(x,y,z) \geq 0) \\ |\omega_i(x,y,z)| & (\omega_i(x,y,z) < 0), \end{cases} \tag{5}$$

$$\omega_{+i}(x,y,z) = \begin{cases} |\omega_i(x,y,z)| & (\omega_i(x,y,z) > 0) \\ 0 & (\omega_i(x,y,z) \leq 0). \end{cases} \tag{6}$$

$$(\omega_{-i}(x,y,z) \geq 0,\ \omega_{+i}(x,y,z) \geq 0)$$
$$(i = x, y, z)$$

The examples of visualization using the proposed method are shown in the following section 4. The location and representative quantities of each resolved vortex are simply represented with a mark and its size or coloring, respectively. In the conventional visualization analysis, the analysis of the time variation of the vortex structure requires many figure because the analysis for one instantaneous flow field requires at least of one figure, as shown in Fig. 8. In addition, it is difficult to accurately evaluate the position and characteristics of each vortex. Using the visualization method, evaluate the characteristic or time variation of the flow structure by drawing the location and feature values of resolved vortices extracted by the proposed method for multiple time steps on a single figure.

3 Analysis target

Here, we investigate the effectiveness of the proposed method by applying to the LES dataset of a transient flow around an airfoil, which is controlled by a DBD plasma actuator [11]. The airfoil is the NACA0015 with an aspect ratio of $s/c = 0.2$ (s:span length, c:chord length). The DBD plasma actuator is installed on the airfoil surface at $x/c = 0.05$ of the chord length from the leading edge. The Reynolds number based on the chord length is $Re = 63,000$. This Reynolds number corresponds to the chord length $c \approx 0.1$[m] and the free-stream velocity $U_\infty \approx 10$[m/s] in the actual experimental conditions [12]. The specific heat ratio and the Prandtl number are set at $\gamma = 1.4$ and $Pr = 0.72$. If the Mach number is relatively lower, the convergence of the numerical solution is decreased. In order to avoid the problem, it is preferable to select a Mach number that has a low compression effect and a high convergence of numerical solution. Therefore, the free-stream Mach number is set at $M = 0.2$. The validity of the Mach number was examined by Asada et al [13]. The angle of attack is set at $\alpha = 12°$, which is higher than the stall angle $\alpha = 11°$. It is known that the use of unsteady actuations with intermittently changing the ON and OFF for the actuation of the DBD plasma actuator , which is called "burst mode actuation [14]", gives better separation control effect at this Reynolds number as compared to the continuous mode actuation. Therefore, the burst mode actuation is used for the separation control. In this study, the LANS3D solver [15] is employed for the large-eddy simulation. The three-dimensional compressible Navier-Stokes equations were solved in generalized curvilinear coordinates. A C-type structured grid is used for the numerical computation and outputting of the numerical dataset, as shown in Fig. 7. The validation and verification of the computational approach is described in the previous study [16]. No-slip conditions were adopted to the airfoil surface and a periodic boundary condition was applied to the boundaries in the spanwise direction.

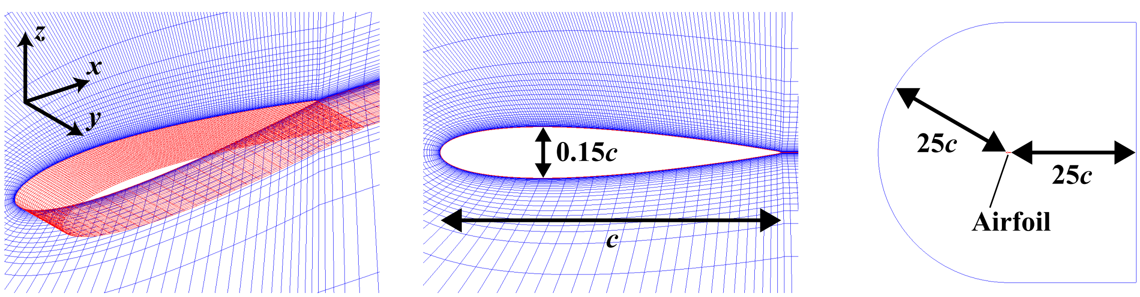

Figure 7 Computational grid for outputting the numerical dataset.

Figure 8 shows the instantaneous flow fields in separation (un-controlled flow, time: $t = T_1$), transition (flow in which control is in progress, $t = T_2$, T_3, *and* T_4), and attached (controlled flow, time: $t = T_5$) phase. The isosurfaces represent the second invariant of the velocity gradient tensor (Q^*) colored with the chordwise velocity. In the separation phase which is the uncontrolled flow, the flow is separated from the airfoil surface. In the transition phase when the separation control is progressing, the flow is gradually attached from the leading edge. In the attached phase when the separation control is sufficiently achieved, the flow is attached to the airfoil surface. Previous studies [16, 17] have confirmed that the flow attachment achieves the lift improvement and drag reduction. However, the factors that promote the flow attachment are not always that obvious. In this study, we analyzed the characteristics and time variation of resolved vortices from the separation phase to the attached phase by using the proposed method.

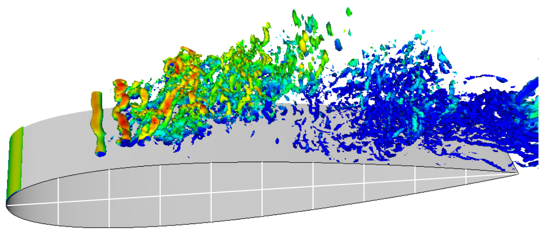

(a) Separation phase ($t = T_1$).

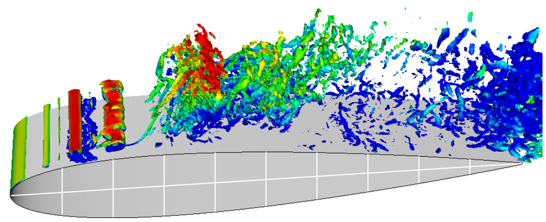

(b) Transition phase ($t = T_2$).

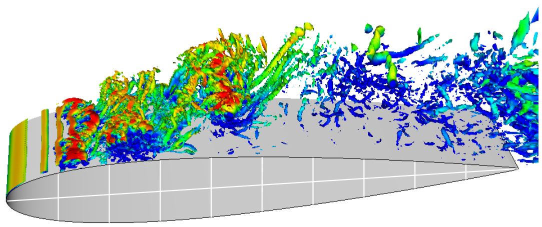

(c) Transition phase ($t = T_3$).

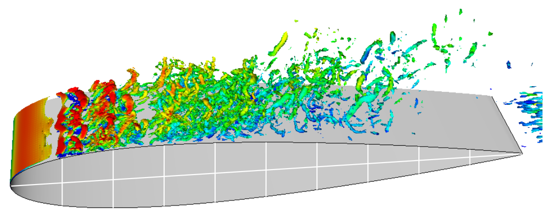

(d) Transition phase ($t = T_4$).

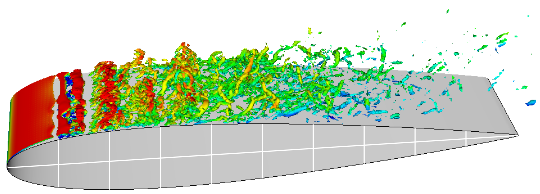

(e) Attached phase ($t = T_5$).

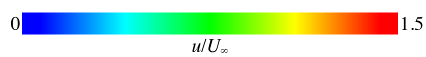

Figure 8 Vortex structures visualized by Q^*(=100) at instantaneous flow fields in each phase.

4 Results and discussion

4.1 Visualization of vortex filaments

Figure 9 shows the vortex filaments extracted by the proposed method of the instantaneous flow fields at the separation phase ($t = T_1$). The coloring only distinguishes each filament and has no physical meaning. The vortex filaments are distributed as the distribution of the vortex structure, as shown in Fig. 8(a). (Note: The spline interpolation of Q^* is performed between the points during the vortex structure visualization process. Therefore, vortex filaments may not be shown at all the vortex structure is drawn. In addition, the periodic boundary was handled as the wall in this study, but by acquiring the physical quantity around the point on the periodic boundary, the Q^* can be calculated and the vortex filament can be extracted across the periodic boundary.)

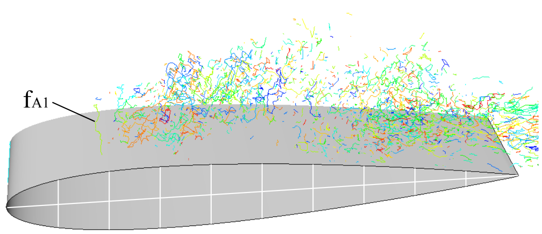

(a) Overview.

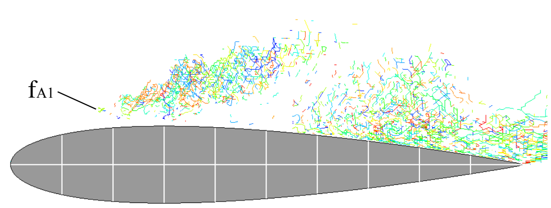

(b) Sideview.

Figure 9 The vortex filaments extracted by the proposed method at the separation phase ($t = T_1$).

Figures 10(a) and 10(b) show vortex filaments (white lines) and the vortex structure represented by the isosurface of Q^* and the cross sections of Q^*, respectively. The vortex filament penetrates the high Q^* region in vortex structures. The two-dimensional vortex structure ($\mathrm{V_A}$) consists of two resolved vortices (and two vortex filaments). The first and second vortex filament is $\mathrm{f_{A1}}$ which extends long from the front of the image to the back and $\mathrm{f_{A2}}$ which extends slightly to the back, respectively. The reason why the vortex filaments ($\mathrm{f_{A1}}$ and $\mathrm{f_{A2}}$) are separated into two is due to the method of selecting the paths in Step 5 of the algorithm in subsection. 2.1. In other words, the integral value of the other path was higher than the integral value of the path connecting $\mathrm{f_{A1}}$ and $\mathrm{f_{A2}}$.

The collapsing two-dimensional vortex structure ($\mathrm{V_B}$) is composed of several resolved vortices and an equal number of vortex filaments. These vortex filaments are separated from each other in the middle of the two-dimensional vortex structure. The collapse of the two-dimensional vortex structure can be inferred from this result alone. Some spiral vortices [18] are confirmed which branched from the two-dimensional vortex structure can be observed from $\mathrm{V_B}$ and its occurrence of this branch is due to the characteristic of $\mathrm{V_B}$. In other words, if the vortex structure is represented by Q^*, the vortex structure may have a branching structure. $\mathrm{f_{B1}}$ and $\mathrm{f_{B2}}$ show the characteristics of vortex filaments where the vortex structure branches. $\mathrm{f_{B1}}$ penetrates through the two-dimensional vortex structure and then enters the branched vortex structure ($\mathrm{V_C}$). $\mathrm{f_{B2}}$ penetrates through the two-dimensional vortex structure but is not connected to $\mathrm{f_{B1}}$. Thus, each vortex filament extracted by the proposed method does not have a branching structure. As a result, the vortex filaments were successfully extracted with the proposed method.

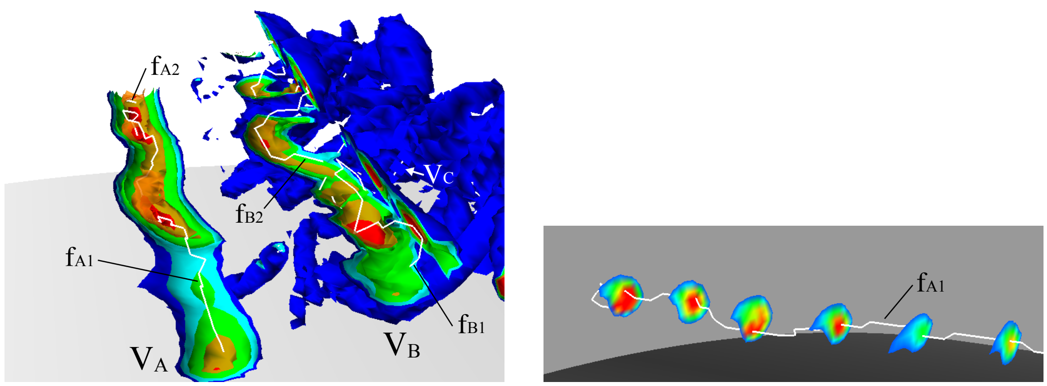

(a) The vortex structures are represented by the isosurfaces of Q^*.

(b) The vortex structure is represented by the cross sections of Q^*.

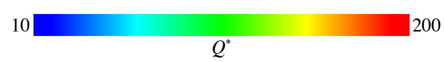

Figure 10 The vortex filaments (white lines) extracted by the proposed method and the vortex structures represented by Q^* at the separation phase ($t = T_1$).

4.2 Characteristics analysis for resolved vortices in the quasi-steady flow phases

Figure 11 shows the characteristics and spatial distribution of the resolved vortices in the separation (left side, $t \leq T_1$) and attached (right side, $T_5 \leq t$) phase. The result is generated from the three-dimensional volume dataset and is overlapped in spanwise direction. The location and size of the circles represent the center of gravity and the volume of the resolved vortex, respectively. The coloring of the circle is determined by the maximum component of the vorticity vector line- integrated along the vortex filament, as shown in Fig. 11. Fine-scale vortices are extracted from 50 instantaneous flow fields acquired at time interval of $\Delta t = 0.02 \times c/U_\infty$ within a certain time range in each phase (separated phase: $T_1 - c/U_\infty < t \leq T_1$, attached phase: $T_5 \leq t < T_5 + c/U_\infty$). In addition, in Fig. 11(a), a suction surface of the NACA0015 airfoil and a shear layer thickness at the separation phase are drawn with a black line and black broken line, respectively. Both separation and attached phases are quasi-steady. Therefore the resolved vortices are distributed in a certain region. In the separation phase, the distribution of resolved vortices is centralized on the shear layer and the trailing edge. Near the shear layer, the resolved vortices with a high vorticity magnitude and a high positive spanwise vorticity components ($\omega_{+y} > \omega_{+x,-x,-y,+z,-z}$) are distributed. Near the trailing edge, the resolved vortices with a high vorticity component other than the positive span direction are distributed. In the attached phase, the resolved vortices with a smaller volume are distributed in a region closer to the airfoil surface than in the separated phase. Near the leading edge, the resolved vortices with a very high vorticity magnitude and a high positive spanwise vorticity are distributed. Near the middle chord, the vorticity magnitude decreases overall. Nevertheless, the resolved vortices maintain a high proportion of the large positive spanwise vorticity. Near the trailing edge, the resolved vortices with a very small volume are distributed. The resolved vortices with the high positive spanwise vorticity are outstanding by the separation control with the plasma actuator.

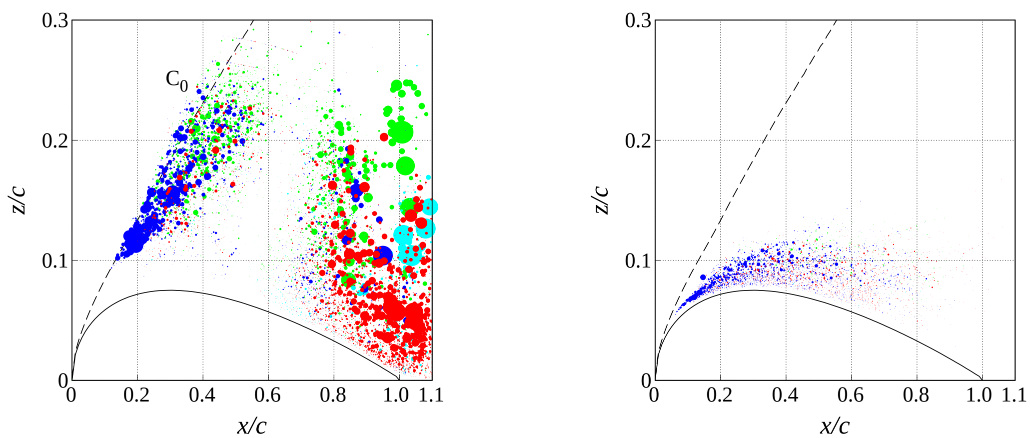

(a) The spatial distribution of the resolved vortices.

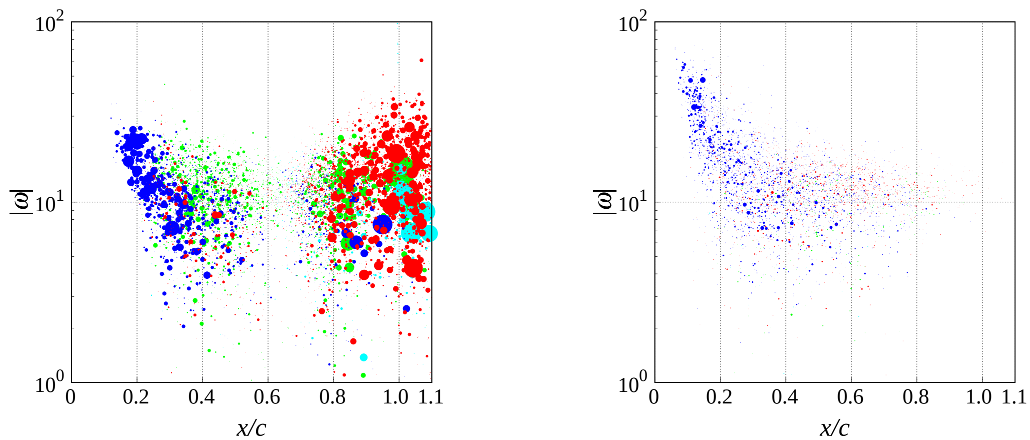

(b) The vorticity magnitude of the resolved vortices.

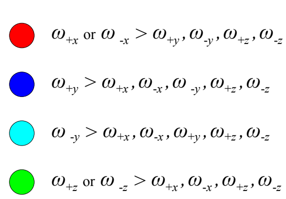

Figure 11 Characteristics of the resolved vortices at the separation (left side) and attached (right side) phases.

4.3 Time variation analysis for the resolved vortices in the unsteady flow phase

Figure 12 shows the time variation of the resolved vortices with a high positive spanwise vorticity component (left side) and the other resolved vortices (right side) from the separation phase ($t = T_1$) to the transition phase (from T_1 to T_4). The result is generated from the three-dimensional volume dataset and is overlapped in spanwise direction. The time scale is the same as the one used in Fig. 8. The location and size of the circles represent the center of gravity and the volume of the resolved vortex, respectively. The coloring of the circle represents the time variation. In addition, the suction surface of the NACA0015 airfoil and the shear layer thickness in the separation phase are drawn with a black line and a black broken line, respectively. From T_1 to T_2, the actuation vortex V_1 which is generated by the drive of the DBD plasma actuator is shed from the leading edge. V_1 moves along the shear layer at the separation phase. A cluster of the resolved vortices C_0 which was distributed along the shear layer at the separation phase is pushed by V_1 toward the airfoil surface. After the shedding of V_1, a new actuation vortex V_2 is shed from the leading edge by the second drive of the DBD plasma actuator. From T_2 to T_3, V_2 moves closer to the airfoil surface than V_1. In addition, a new cluster of the resolved vortices $\mathrm{C}_{1,2}$ is generated at the trajectory that V_1 and V_2 passed. C_0 is pushed further toward the airfoil surface by V_1 and V_2. After the shedding of V_2, a cluster of actuation vortices C_3 is shed from the leading edge by the third drive of the DBD plasma actuator. From T_3 to T_4, C_3 moves closer to the airfoil surface than V_2. C_0 disappears, and $\mathrm{C}_{1,2}$ come closer to the airfoil surface. After T_4, V_1, V_2, and $\mathrm{C}_{1,2}$ move away from the airfoil and only C_3 remains. Finally, the separation control is achieved.

These obtained results suggest that the actuation vortices with the high positive spanwise vorticity component promotes the flow attachment. The actuation vortices move while pushing the surrounding vortex cluster toward the airfoil surface. The newer actuation vortex moves closer to the airfoil surface than the older actuation vortices. As the flow condition approaches the attached phase, the actuation vortex collapses near the leading edge and becomes the vortex cluster. The vortex cluster moves closer to the airfoil surface than the older activation vortices. Eventually, the vortex cluster is distributed on the airfoil surface, and the flow condition shifts to the attached phase. These results are difficult to obtain only by using the conventional visualization analysis method, as shown in Fig. 8, and the effectiveness of the proposed method was shown.

5 Conclusions

In this study, we established a vortex structures analysis method for the large-eddy simulation (LES) data. In the proposed method, the vortex structure region is determined using the second invariant of the velocity gradient tensor, and the vortex filaments are extracted from the region to identify the resolved vortices (fine-scale vortex structures) and evaluate their feature values. By using the feature values, it is possible to perform characteristic analysis for steady flow and time variation analysis for unsteady flow, as well as statistical analysis and cluster analysis. To investigate the effectiveness of the proposed method, it was applied to actual LES dataset that is a transient flow around an airfoil, which is controlled with a DBD plasma actuator. As a result, the vortex filaments and resolved vortices were successfully identified and their location, volume, and vorticity components were evaluated. Each resolved vortex was color-coded by the feature value, and the distribution of vortices in steady flow and the trajectory of individual vortices in unsteady flow were analyzed. These results were difficult to obtain only by using the conventional visualization analysis method, and the effectiveness of the proposed method was shown. However, the proposed analysis method does not strictly distinguish each resolved vortex. Furthermore, the analysis method is required to evaluate in detail the effect on the resolved vortex to the surrounding flow structure. In a future study, we will propose a new analysis method for tracking the resolved vortex and other structures and evaluating their time variation. In addition, we will propose the new analysis methods for clustering the fine-scale flow structures and evaluate the relationship between the large-scale flow structure and the fine-scale flow structure.

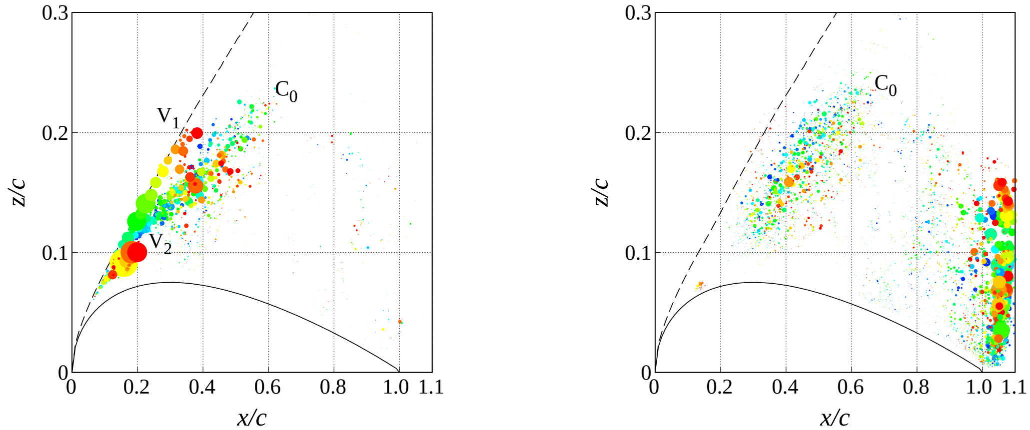

(a) From T_1 to T_2.

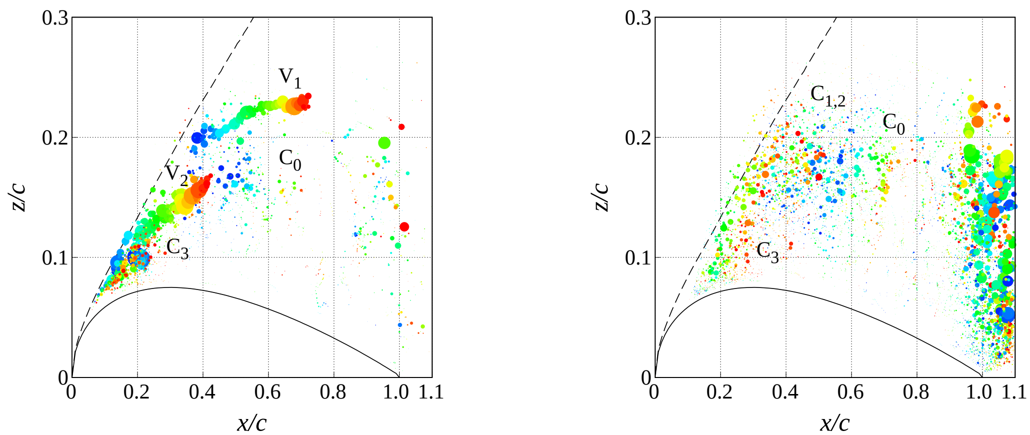

(b) From T_2 to T_3.

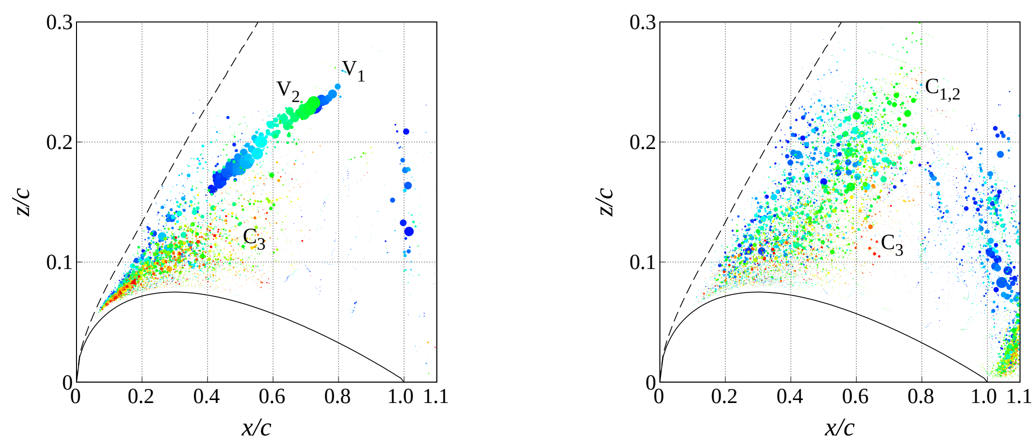

(c) From T_3 to T_4.

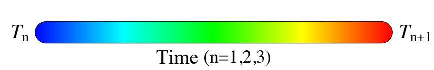

Figure 12 Time variation of the resolved vortices with a large positive spanwise vorticity component (left side) and the other resolved vortex (right side) during the transition phase (from T_1 to T_4).

Acknowledgement

The research was supported by the JSPS Grant-in-Aid for Scientific Research No. 18H03816 in Japan. The computations in this study were performed using the JAXA 460 Supercomputer System Generation 2 (JSS2) at the Japan Aerospace Exploration Agency.

References

[1] J.C.R. Hunt, A.A. Wray, and P. Moin, "Eddies, streams, and convergence zones in turbulent flows," Studying Turbulence Using Numerical Simulation Databases, N89-24555, pp. 193-208, 1988.

[2] M.S. Chong, A.E. Perry, and B.J. Cantwell, "A general classification of three- dimensional flow fields," Physics of Fluids A: Fluid Dynamics, 2(5), 765, 1990.

[3] J. Jeong and F. Hussain, "On the identification of a vortex," Journal of Fluid Mechanics, 285, pp. 69-94, 1995.

[4] L. Graftieaux, M. Michard, and N. Grosjean "Combining PIV, POD and vortex identification algorithms for the study of unsteady turbulent swirling flows," Measurement Science and Technology, 12(9), 1422, 2001.

[5] R.D. Moser and M.M. Rogers, "Mixing transition and the cascade to small scales in a plane mixing layer," Physics of Fluids A, 3(5), pp. 1128-1134, 1991.

[6] H. Miura and S. Kida , "Identification of Tubular Vortices in Turbulence," Journal of the Physical Society of Japan, 66(5), pp. 1331-1334, 1997.

[7] T. Wang, M. Tanahashi, and T. Miyauchi, "Coherent fine scale eddies in turbulence transition of spatially-developing mixing layer," International Journal of Heat and Fluid Flow, 28(6), pp. 1280-1290, 2007.

[8] J. Jiménez and A. A. Wray, "On the characteristics of vortex filaments in isotropic turbulence," Journal of Fluid Mechanics, 25(373), pp. 255-285, 1998.

[9] T. Makihara, S. Kida, and Miura H, "Automatic tracking of low-pressure vortex," Journal of the Physical Society of Japan, 71(7), pp. 1622-1625, 2002.

[10] C. Liu1, Y. Gao, S. Tian, and X. Dong, "Rortex - A new vortex vector definition and vorticity tensor and vector decompositions," Physics of Fluids, Vol. 30, Issue 3, 2018.

[11] T.C. Corke, C.L. Enloe, and S.P. Wilkinson. "Dielectric barrier discharge plasma actuators for flow control," Annual Review of Fluid Mechanics, 42, pp. 505-529, 2010.

[12] S. Sekimoto, T. Nonomura, and K. Fujii, "Burst-Mode Frequency Effects of Dielectric Barrier Discharge Plasma Actuator for Separation Control," AIAA Journal, Vol. 55, No. 4, pp.1385-1392, 2017.

[13] K. Asada, " Computational Analysis of the Flow Fields Induced by a DBD Plasma Actuator Toward Separated-Flow Control, " Ph.D. Thesis, University of Tokyo, Tokyo, 2014.

[14] K. Fujii, "Three flow feature behind the flow control authority of DBD plasma actuator: Result of high-fidelity simulations and the related experiments," Applied Science 2018, 8(4), 546, 2018.

[15] K. Fujii, H. Endo, and M. Yasuhara, "Activities of Computational Fluid Dynamics in Japan: Compressible Flow Simulations," High Performance Computing, pp. 139-161, John Wiley & Sons, New York, 1990.

[16] M. Sato, T. Nonomura, K. Okada, K. Asada, H. Aono, A. Yakeno, Y. Abe, and K. Fujii, "Mechanisms for laminar separated-flow control using dielectric-barrier-discharge plasma actuator at low Reynolds number," Physics of Fluids, 27(11), 117101, 2015.

[17] T. Ogawa, K. Asada, T. Tatsukawa, K. Fujii, "Analysis of Transient Flows over an NACA0015 Airfoil toward Better Flow Control Authority of Plasma Actuators," 17th European Turbulence Conference, No. 474, Torino, Italy, 2019.

[18] G. Kawahara, S. Kida, M. Tanaka, and S. Yanase, "Wrap, tilt and stretch of vorticity lines around a strong thin straight vortex tube in a simple shear flow," Journal of Fluid Mechanics, Vol. 353, pp. 115-162, 1997.